論文 / 著書情報
Article / Book Information

Title	Liquefaction-induced deformation of earthen embankments on non-homogeneous soil deposits under sequential ground motions
Authors	Manika Maharjan, Akihiro Takahashi
Citation	Soil Dynamics and Earthquake Engineering, Vol. 66, pp. 113-124
Pub. date	2014, 11
DOI	http://dx.doi.org/10.1016/j.soildyn.2014.06.024
Creative Commons	See next page.
Note	This file is author (final) version.

License

Liquefaction-induced deformation of earthen embankments on non-homogeneous soil deposits under sequential ground motions

Manika Maharjan and Akihiro Takahashi[1]

Department of Civil Engineering, Tokyo Institute of Technology, 2-12-1 O-okayama, Tokyo 152-8552, Japan

Abstract

Damage of embankments during earthquakes is widely attributed to the liquefaction of foundation soil. Previous studies have investigated the dynamic response of embankments by mainly considering uniform sand foundation and a single earthquake event. However, the foundation of an embankment consists of many sublayers of soil from liquefiable sand to relatively impermeable layer, and during earthquakes a mainshock may trigger numerous aftershocks within a short time which may have the potential to cause additional damage to soil structures. Accordingly, the investigation of liquefaction-induced deformation of earthen embankments on various liquefiable foundation conditions under mainshock-aftershock sequential ground motions is carried out by a series of dynamic centrifuge tests in this study. The liquefiable foundation includes uniform sand profile, continuous layered soil profile, and non-homogeneous soil profiles. Effects of various foundation conditions on embankment deformations are compared and analyzed. From the test results, it is found that the embankment resting on non-homogeneous soil deposits suffer more damage compared to the uniform sand foundation of same relative density. The test results also suggest that the sequential ground motions have a significant effect on the accumulated deformation of embankment.

Key words: *liquefaction, embankment, deformation, non-homogeneous foundation, centrifuge model test, excess pore water pressure.*

Soil Dynamics and Earthquake Engineering, 66, 113-124, 2014

Official URL:

http://dx.doi.org/10.1016/j.soildyn.2014.06.024

[1]Corresponding author.

Email address: takihiro@cv.titech.ac.jp (A. Takahashi)

1. Introduction

Earthquake induced liquefaction has become a major problem to soil embankments such as river dykes, levees, road embankments and earth dams, supported on a cohesionless foundation soil. Previous studies have shown that the widespread damage to such embankments occurred mainly due to the liquefaction of foundation soil, resulting in cracking, settlement, slumping and lateral spreading [1-5].

Several experimental studies and numerical analyses have been conducted previously to examine the behavior of embankments resting on uniform clean cohesionless soil during earthquakes [2,4,6,7]. Previous studies that proposed various techniques for mitigation of liquefaction-induced damage in uniform ground have also been reported [4,7]. It is noted however, that natural sand deposit normally consists of many sublayers with different soil particles and properties, ranging from soft sand lenses to stiff cohesive clay and coarse sand layers, referred to as non-homogeneous soil deposits (Fig. 1). Kokusho and coworkers [8,9] have studied the formation of water film beneath the thin impermeable silt due to difference in permeability in layered sand and its role in the extent of lateral deformation in the sloping surface. Malvick and coworkers [10,11] conducted centrifuge tests to demonstrate the shear localization due to void redistribution and its consequences on large postshaking deformations in a sand slope with continuous embedded silt layers. In a previous study [12,13] we conducted centrifuge model tests and numerical analyses to investigate the liquefaction mechanism in non-homogeneous soil deposits. Non-homogeneous soil deposits were modeled based on the features of actual soil profile with discontinuous low permeability layers in multi-layered sand deposits. Non-homogeneity in foundation was incorporated by including periodically distributed silty sand patches of a lower permeability than the liquefiable sand. It was found that excess pore water pressure remains for a longer period of time at discontinuous regions in non-homogeneous soil deposits compared with the continuous layered and uniform soil deposits, manifesting a larger settlement at that corresponding region causing non-uniform settlements. Nonetheless, most of the embankments rest on non-homogeneous liquefiable soil profiles, which consist of thin layers of discontinuous low permeability layers like silty sand or clay. Oka et al. [14] performed numerical modeling of river embankments on a foundation with various soil profiles and ground water tables, including a clayey soil layer. However, most previous studies have only investigated the dynamic behavior of embankments resting on uniform sand. Thus, the dynamic behavior of earthen embankments on a liquefiable non-homogeneous foundation, consisting of discontinuous low permeability layers of silt or clay at different depths is not well understood. Despite the extensive research and development of remedial measures to prevent the large deformation of soil structures, embankments have suffered severe damage during past earthquakes. During 2011 Great East Japan Earthquake, Japan's Ministry of Land, Infrastructure, Transport, and Tourism (MLIT) documented that more than two thousand locations of levee suffered some level of damage [14,15]. The minor to major damage was attributed due to the liquefaction of foundation soil. This event elucidates the further need to understand the deformation behavior of embankment resting on non-homogeneous liquefiable foundations.

Repeated ground-motion sequences occurring after short intervals of time, resulting from mainshock-aftershock earthquakes, have been observed during many earthquakes [16]. Previous studies have pointed out that the low-amplitude aftershock can accumulate large lateral deformation and continue for several minutes on the liquefied soil [17-19]. Ye et al. [20] conducted shaking table tests and numerical analyses on saturated sandy soil to investigate the mechanical behavior of liquefiable foundations during repeated shaking and consolidation. Xia et al. [21] presented numerical analysis of an earth embankment on liquefiable foundation soils under repeated shake-consolidation process. However, in most of the previous experimental and numerical studies seismic performance of soil structures is investigated by applying only a single earthquake, ignoring the influence of repeated earthquake phenomena. During 2011 Great East Japan Earthquake, the liquefaction-vulnerable structures continued to shake after the onset of soil liquefaction for more than two minutes. Moreover, during the reconnaissance survey after 2011 Great East Japan Earthquake, Sasaki and his team [22] found that the more severe deformation and subsidence of levees was due to the occurrence of aftershock, 30 minutes after the mainshock. Moreover, no previous study has examined the effects of repeated earthquakes on embankments lying on non-homogeneous soil deposits. Therefore, to understand the deformation mechanism of embankments lying on non-homogeneous soil deposits under mainshock and sequential ground motion is of great importance.

This paper presents the results of dynamic centrifuge tests conducted on different foundation conditions: one involving a uniform foundation; one involving a continuous silty sand layer foundation; and three involving non-homogeneous discontinuous silty sand layer foundations. The work presented herein compares the liquefaction-induced deformation of embankments resting on different foundations under mainshock and sequential ground motion.

2. Centrifuge testing program

Five dynamic centrifuge tests were conducted on three different liquefiable foundations utilizing the Tokyo Tech Mark III centrifuge of radius 2.45 m, at a centrifugal acceleration of 40g. The model configurations and the entire test results are presented and discussed in prototype scale units, unless indicated otherwise. All tests simulated a prototype soil deposit of 8.4 m depth and embankment of 1.2 m height. Toyoura sand and Silica sand No. 8 was used in the tests to model the foundation (Table 1). It is noted that Toyoura sand, also referred to as fine sand, was deposited at a relative density $D_r \approx 50\%$. Silica sand No. 8, also referred to as silty sand, was deposited at a relative density $D_r \approx$ 50-55%, and used to create the relatively impermeable layer in layered soil profiles. DL clay, which consists of 90% silt and 10% clay, was mixed with 22% silicon oil by weight to build the embankments, with 1:2 slopes having a unit weight of 16 kN/m^3. The model configurations are shown in Fig. 2 and Table 2: Model NHG1 and Model NHG2 simulate non-homogeneous foundations consisting of fine sand layers with two discontinuous silty sand layers of thickness 1.0 m (Fig. 2(a) and (b)); Model UG simulates homogeneous uniform sand foundation consisting of only Toyoura sand (Fig. 2(c)); Model CG simulates non-homogeneous soil deposit with continuous silty sand layers (Fig. 2(d)). An additional test, Model

NHG1-MS was also conducted, which consists of the same non-homogeneous foundation as Model NHG1, but only having a mainshock applied.

A flexible laminar container with inner dimensions of 500×200×450 mm in length, width, and height, respectively was used to build the models. The box is composed of 20 aluminum alloy rectangular rings which allow the container to move with the soil, creating a flexible boundary and ensuring the uniform distribution of dynamic shear stresses within the soil. The foundation was prepared by air pluviation to a depth of 210 mm in model scale. The sand was poured from a hopper which was manually moved back and forth along the longest dimension of the box, while the falling height was kept constant to obtain the desired relative density. During the preparation of non-homogeneous soil deposits, Toyoura sand was deposited first and then, the remaining parts were filled with Silica sand No. 8 (Fig. 2(c) and (d)). Trapezoidal silty sand patches were chosen to model the multi-layered soil profile consisting of discontinuous thin layers of low permeability observed in many damaged sites during past earthquakes [23,24]. After the foundation was constructed, the embankment was built of a mixture of DL clay and silicon oil with 1:2 slopes. The models were saturated with a viscous fluid, i.e., a mixture of water and 2% Metolose (Hydroxypropylmethyl cellulose from Shin-Etsu Chemical Company) by weight of water, to achieve a viscosity of about 40 times the viscosity of water. The density and surface tension of this solution is practically identical to that of water [17]. Also, the viscous fluid simulates the actual prototype permeability of the soil. The de-aired Metolose solution was dripped slowly from the top of the container under a vacuum of 760 mmHg which slowly moves downwards. In this process, the water table rises from the bottom. The saturation was continued until the solution level reached the elevation of 210 mm in model scale, i.e., the water table is at the free field surface. The saturation process for all the tests required approximately 30 hours. It is noted that the soil layers in all the models were leveled and horizontal. Considering the rotational direction, the ground surface has to be curved in the plane parallel to y direction (the direction perpendicular to the embankment section) in Fig. 2 and the elevation at the center should be 2.8 mm lower than that at the edges of the container. However, since there was no obvious spreading on the ground in the direction perpendicular to the embankment section due to shaking, its effects were neglected.

Accelerometers and pore pressure transducers (PPTs) were installed during model preparation to measure the accelerations and excess pore water pressure (Δu) generated at three regions representing different stress states: (1) free field; (2) under the toe of the embankment where static shear stress exists; and (3) under the center of embankment where large effective stress exists. Colored noodles were placed both vertically and horizontally at several locations to trace the deformation pattern within the foundation layer. The horizontal noodles were placed at the sand-silt interface. The vertical noodles of 1.5 cm were placed at several locations (1.2, 3.6, 6, 7.2, 9.5 m) along the x-axis at several depths. Also, markers made up of small nails were aligned at the center on the ground surface and several locations on embankment to map the deformations. Finally, laser displacement transducers (LDTs) and potentiometers were placed at the embankment crest and free field surface. The locations of accelerometers, PPTs, LDTs, and potentiometers are indicated in Fig. 2.

All the models except NHG1-MS were subjected to the same sequential earthquake ground motion, consisting of a mainshock and aftershock, recorded at the Moorpark-Fire station (EW component) during 1994 Northridge earthquake [25], normalized to maximum PGA equal to 0.4 g (for the mainshock). Table 2 indicates the peak acceleration of input motion observed in the centrifuge test for all the models. A gap of 100 s is applied between two consecutive seismic events. This gap has zero acceleration ordinates. In Fig. 3, the ground motion applied to the shaker is plotted with a dotted line, and the input motions recorded at the base of the laminar container for each test are plotted with solid lines. Figure 4 depicts the Fourier spectra and Arias intensity of the input base motions. The waveform simulated by the shaker is not identical to that of the Northridge earthquake, but similar in the time domain (Fig. 3) and agrees fairly well in the frequency domain as shown by Fourier spectra in Fig. 4, except for Model NHG2. Also, the Arias intensity of all the input motions appear to be similar. Repeatability of applied earthquake motion for all cases was satisfactory, except for the test NHG2, where the intensity of applied input motion was less than other tests.

After completion of the tests, the final locations of markers aligned on the ground surface and embankments were carefully measured. Dissections of models were also carried out to measure the final locations of the noodles placed at different positions, accelerometers, and PPTs. The post-test deformed shapes of the model cross section were then obtained by carefully mapping the measured coordinates of noodles, markers, and transducers. Selected response records in prototype units will be presented in following sections.

3. Test results and analyses

3.1. Model NHG1

Figure 5(a) depicts the mapped post-test deformed shape of Model NHG1. The time histories of displacements at LV1 and PM1 and accelerations at A12 and A13 (see Fig. 2 for locations of these points) for the model NHG1 are presented in Fig. 6. Here a crest settlement of 0.5 m (about 40% of the embankment height) was observed of which about 0.34 m was measured during the mainshock shaking (Figs. 5(a) and 6). Slumping of embankment sides and the lateral spreading of 0.4 m at the toe portion were observed, where the ground surface was observed to heave upward by as much as 0.2 m (Fig. 5(a)). The lateral outflow of underlying foundation soil toward the free field, shear deformation of embankment, and contractive volume change of loose sand under embankment are largely responsible for the larger crest settlement. The lateral deformation may be associated with an average normal tensile strain of about 10% along the embankment base. In addition, tension cracks occurred at the crest and side of the embankment in the direction perpendicular to the embankment section, which might be due to the extension of the embankment as the lateral spreading of underlying foundation soil occurred. Major cracks of width 0.3 m were observed at the crest and cracks of width 0.1 m at the embankment sides (Fig. 5(a)).

A significant amount of crest settlement took place during mainshock shaking, presumably larger during 8-20 s with a heave of about 0.12 m at PM1 as shown in Fig. 6. When the excess pore water pressure, Δu reaches a value equal to the initial vertical effective stress, σ' i.e., excess pore water pressure ratio, r_u approaches unity, $r_u = \Delta u / \sigma'$) liquefaction occurs. Initial vertical effective stresses due to embankment loadings were calculated based on the influence values assuming the foundation ground to be elastic semi-infinite as proposed by Osterberg [26]. Pore water generated rapidly in a few cycles at all depths (Fig.7). The maximum r_u values at all depths are included in Fig. 7. The r_u values were largest at the free field and lowest below the embankment throughout the shaking. The rapid liquefaction in the free field might have reduced the confinement of the soil below the embankment and might have allowed the lateral stretching of the soil below the embankment towards the free field. Under nearly undrained condition, this tensile strain mechanism suppressed the increase of excess pore water pressure in the soil below the embankment. This effect was more prominent near the center line as the embankment and its foundation ground was symmetric, causing lower r_u values below the embankment. Also, the r_u was limited to lesser values due to the presence of initial shear stress in the soil below the embankment [27,28]. Such lower r_u values below the embankment were also reported by [2,4,29,30]. As the r_u value was larger at the bottom stratum, the accelerations were highly attenuated relative to the base input. In the free field, the attenuation of acceleration was significant after a few cycles due to the loss of soil stiffness and strength. However, some asymmetric acceleration spikes appeared below the embankment toe at A13, where high initial static shear stress existed (Fig. 6). Such asymmetric spiky acceleration responses has been investigated by many researchers (Dobry et al. [31], Elgamal et al. [32]) which depict the occurrence of cyclic downslope deformations towards the free field, further suggesting the maximum shear strain at the toe region. Moreover, large strains were attained near the toe region and relatively small strains below the embankment centerline. Figure 8 indicates the maximum shear strain amplitude observed in the centerline at different depths during mainshock and aftershock. Shear strain amplitude at several locations during shaking was calculated by using acceleration time histories, based on the method by Koga and Matsuo [2] and Elgamal et al. [32]. The pore water was accumulated beneath the silty sand layer as the silty sand layer acted as the barrier for vertical dissipation of excess pore water pressure. As a result, formation of dilation zone beneath the low permeability silty layer might occur, isolating the silty layer and the lateral deformation was observed at the bottom of the silty sand layer. Shear strain amplitudes were larger at the bottom of the silty sand layer as seen in Figs. 5 (a) and 8. It is noted that the middle sandy layer above the silty sand layer translated sideways without much internal shear deformation. However, the shear deformation was continuous as depth decreases at the bottom sand portion.

Shear deformation of embankment due to shear deformation of underlying liquefied sand is also a significant factor for crest settlement. Generally, the change in volume of embankments is expected to be small [33]. It is noted that no slope failure of the embankments was detected during the tests presented in this paper. Assuming the volume change of the embankments due to

shaking to be negligible, the vertical strain at the top of embankment becomes equal to the horizontal strain at the embankment base. Thus, the crest settlement due to shear deformation of embankment is expressed as the product of horizontal strain of embankment base and its height. For example, in Model NHG1, crest settlement due to shear deformation = 0.1 x 1.2 =0.12 m, where horizontal strain of embankment base =10% and height of embankment=1.2m.

Volumetric change due to pore water dissipation is also a factor for crest settlement along with the initiation of earthquake loading and generation of Δu and its dissipation. Closer examination of the recorded Δu during the mainshock shaking revealed the gradual increment of Δu under the embankment, i.e., at P5, P9, and P10 (Fig. 7). The migration of pore water might also have taken place during shaking and this might have caused the continuous and gradual rise of Δu below the embankment centerline (i.e., at P5, P9, P10), contracting the soil. Nonetheless, such gradual increment was not observed in the free field and beneath the toe regions. Moreover, the settlement of PPTs might have contributed partly in the rise of Δu. Evidence of PPT settlement was visible in each of pore pressure plots where the Δu has not returned back to the zero value, i.e., there existed residual excess pore water pressure after dissipation, Δu_r. The calculated Δu_r and the location of PPTs measured after the test indicated that the PPTs below the embankment settled more than that at the free field. Compared to the other models, the r_u values were the largest below the embankment and below the embankment toe throughout shaking (Fig. 7). The larger r_u values were associated with the larger cyclic shear strain (Fig. 8) and tendency to contract, causing large crest settlement.

Shown in Fig. 9(a) are the recorded time histories of displacements at the crest and free field and Δu at 0.75 m depth. The rise in Δu further occurred under the application of small aftershock, re-liquefying the soil at free field, and causing some additional deformations. The shear strain amplitudes observed during aftershock at different depths were also larger for Model NHG1 (Fig. 8(b)). The deformation occurring after seismic excitation stopped was solely due to the dissipation of Δu. At P10, Δu continued to increase and was significantly larger for a longer period of time. The dissipation of pore water was concentrated through the discontinuity region below the embankment centerline and finally towards the ground surface, contracting the foundation soil below embankment and inducing additional settlement after shaking. As the pore water pressure was dissipated mainly through the discontinuity beneath the embankment in test NHG1, the complete dissipation took a longer period of time, about 1200 s. An additional crest settlement of 0.14 m was measured due to aftershock and dissipation of Δu. The heaving occurring during the mainshock shaking also settled down to a final heave of 0.1 m with the dissipation of Δu. No large deformations took place, but still the overall deformation was large compared to other tests.

3.2. Model NHG2

Figure 5(b) depicts the mapped post-test deformed shape of Model NHG2. Figure 10 shows the displacement time histories during the mainshock. As the intensity of the input motion for this test was comparatively smaller, the deformation was also reduced. A crest settlement of 0.35 m

was observed of which about 0.25 m was measured during the mainshock shaking. Slumping of embankment sides and the lateral spreading of 0.2 m at the toe were observed. An average normal lateral tensile strain was about 5% along the embankment base.

A significant amount of settlement took place during 10-15 s as shown in Fig. 10 which is different from Model NHG1. This might be associated with the rate of Δu build-up. The build-up of Δu was somewhat slower with more cyclic excitation required for liquefaction (Fig. 11), which might be due to the slightly smaller input acceleration. Similar to test NHG1, the soil liquefied at the free field region. However, foundation soil below the embankment centerline was observed to have lower r_u values. i.e., at P10 the maximum r_u value is around 0.15, which is very small (Fig. 11). Also, the gradual decrement in Δu was observed at P10 during shaking, which might be due to the restriction of pore water dissipation through the silty sand layer. This might be attributed to a possible reduction in cyclic shear strain below the embankment (Fig. 8). Also the presence of the upper silty sand layer acted as a hindrance and the water dissipates through the discontinuous region under the toe. The smaller cyclic shear strain might have caused less amount of crest settlement.

Shown in Fig. 9(b) are the recorded time histories of displacements at the crest and free field and Δu at 0.75 m depth during and after shaking. The intensity of aftershock was also significantly reduced, so no big difference in Δu and displacement was observed. The shear strain amplitudes below the embankment centerline were also significantly smaller (Fig. 8(b)). Since P11 was above the discontinuous permeable region, Δu was incredibly large at P11 compared to P10 and P12. This was associated with the hindrance of pore water to transmit through the upper silty sand layer, as the pore water drained through the discontinuous region under the toe. It is noted that the behavior of delayed seepage towards the discontinuity at P11 in Model NHG2 was different from that at P10 in Model NHG1. Despite being the location of both PPTs above the discontinuities, Δu at P11 in Model NHG2 was much lesser and dissipation was quite faster. This might be due to two possible reasons: (a) the presence of two discontinuities at the shallow depth distributes the outflow of water and (b) application of low intensity input motion. The total dissipation of Δu took about 700 s and the heaving occurred during mainshock was recovered.

3.3. Model UG

Figure 5(c) depicts the mapped post-test deformed shape of Model UG. The time histories of displacement at LV1 and PM1, acceleration at A11 and A12 during mainshock are presented in Fig. 12(a). The pattern of deformation was considerably different from other models. The lateral deformation is found to increase continuously towards the ground surface as seen in Fig. 5(c). Nevertheless, the embankment and foundation deformations were reduced compared to other tests. A crest settlement of 0.39 m was observed of which about 0.28 m was measured during the mainshock shaking. The embankment toe was found to laterally spread on both sides towards the free field by 0.2 m. The average normal lateral tensile strain along the embankment base was about 5% which was less than that in Model NHG1. Surface cracking was much less with the largest crack only 0.1 m wide.

The time histories of Δu during the mainshock are presented in Fig. 13. As observed in Model NHG1, the gradual rise of Δu was not observed during the mainshock shaking. The maximum r_u values at P4 and P7 were much lowered compared to Model NHG1 (Figs. 7 and 13). The r_u value is about 0.17 at 10 s, which resulted in the reduced settlement during that period. The lower r_u value below the embankment centerline was associated with the possible reduction in shear strain amplitude (Fig. 8). Also the maximum r_u value after 10 s is 0.27, which is still lower, attributing to the smaller shear strain amplitude. Moreover, the maximum r_u values below the embankment toe, i.e., at P8 is 0.68, which was the major cause for the reduced tendency for lateral deformation. Also, the less significant asymmetric spiky acceleration response at A12 (Fig. 12(a)) was attributed to the reduction in cyclic downslope deformation [31,32]. The lateral outflow of less amount of foundation soil has further reduced the embankment settlement. Although attenuation was occurred, the acceleration just beneath the embankment (A11) was slightly higher than Model NHG1 (A12), attributing to the stiffer foundation (Fig. 12(a)). Moreover, to a small extent, the pore pressure generated at P7 showed a fluctuation or dip (Fig. 13). The appearance of dips has been explained as dilation of soil, indicating a positive volume change, further decreasing the crest settlement [31,33].

Shown in Fig. 14(a) are the recorded time histories of displacements at the crest and free field and Δu at 0.75 m depth in Model UG. Similar to Model NHG1, aftershock caused an increase in Δu generation and an additional settlement with the smaller shear strains below the embankment centerline compared to other tests (Fig. 8(b)). Vertical dissipation took place in the free field and toe region and lateral dissipation occurred under the embankment, consolidating the liquefied soil. For instance, the Δu started decreasing at 200 s at P7, 250 s at P8, and 300 s at P9, which suggested the lateral dissipation mechanism. After shaking, Δu rose slowly below the embankment due to pore water dissipation from the underlying layer [34]. As the permeability of Toyoura sand is large, Δu was fully dissipated in 600 s and the settlement also ceased after 500 s. The heaving of 0.1 m occurring during the mainshock shaking also settled down due to pore water dissipation. An additional crest settlement of 0.1 m was measured due to aftershock and dissipation of Δu.

3.4. Model CG

Figure 5(d) depicts the mapped post-test deformed shape of Model CG. Figure 12(b) shows the time histories of displacement at LV1 and PM1, and acceleration at A12 during mainshock shaking. A crest settlement of 0.45 m was observed of which about 0.32 m was measured during the mainshock shaking. The embankment toe was found to laterally spread on both sides towards the free field by 0.4 m and the ground surface at free field was observed to heave upward by 0.1 m. The lateral deformation may be acquainted with an average normal tensile strain of about 10% along the embankment base. In addition, tension cracks occurred at the crest and side of the embankment in the direction perpendicular to the section of embankment, which might be due to the extension of the embankment as the lateral spreading of underlying foundation soil occurred.

Major cracks of width 0.2 m were observed at the crest and cracks of width 0.1 m at the embankment sides.

Notable shear deformation occurred at the bottom of the silty sand layers. The middle sand layer translated sideways with no shear deformation (Fig. 5(d)). The top sand layer together with the embankment translated sideways. At P10, just below the embankment centerline, Δu increased in a few cycles consisting of several dips and fluctuation as that in Model UG (Fig. 15). At about 9 s, some large dips or fluctuation of pore pressure appeared. This signified dilative stress-strain response, causing a positive volume change which reduced the crest settlement [31,33]. No gradual rise in Δu was monitored below the embankment centerline until 25 s of shaking. Also, the r_u value was significantly smaller at P12 in the free field region throughout the shaking, revealing the soil has not yet liquefied. The non-occurrence of liquefaction indicates the possibility of lack of pore water migration from the underlying layers. After 25 s, a gradual rise in Δu was observed at P10, which might possibly be due to the formation of cracks or vents in the upper silty sand layer around the centerline. Although large attenuation occurred, the acceleration just beneath the embankment (A12) was slightly higher than Model NHG1, attributing to the stiffer foundation (Fig. 12(b)). Maximum lateral deformation of 0.4 m occurred, with equal lateral deformation as that of Model NHG1. As the large shear deformation occurred beneath the top and bottom silty layer, lateral deformation should also occur to a large extent. The lower r_u values at the shallow depth (i.e., above the upper silty layer) at the free field region suppressed the lateral outflow of foundation soil below the embankment.

The recorded time histories of displacements at the crest and free field and Δu at 0.75 m depth during and after shaking in Model CG are presented in Fig. 14(b). A continuous increase in Δu at P10 was observed, similar to Model NHG1, due to the dissipation of pore water through the vent formed around the centerline of the upper silty sand layer. A small aftershock caused rapid increase in Δu, re-liquefying the sand at the free field and beneath the toe. At P10, Δu continued to increase and remained significantly larger until 400 s, while the Δu decreased instantly after the aftershock at P11 and P12. The total dissipation of Δu took about 1200 s and the settlement also continued until 1000 s at a slower rate. An additional crest settlement of 0.11 m was measured due to aftershock and dissipation of Δu.

4. Discussions

In the present study the performance of soil structures such as embankments, levees, and dams is investigated mainly by the movement of structures and the ground supporting it during and after the earthquake. Although, time histories of Δu may be governing factors to estimate the behavior of embankments during an earthquake, eventually the deformations are the most important aspects.

An additional test NHG1-MS was also conducted to investigate the effects of aftershocks on the deformation of embankments. The model configuration is the same as Model NHG1; the difference is that only mainshock shaking was applied. Table 3 indicates the crest settlement occurred in each model during various period of time. Figure 16(a) depicts the normalized crest

settlements during the mainshock relative to Model UG. The crest settlement for Models CG and NHG1 was about 10% and 20% larger than that for Model UG. Also, it is noted that the crest settlement was nearly the same for Models NHG1 and NHG1-MS during the mainshock, which supports the repeatability of the experiment. Based on the theory proposed by Malvick et al. [10] and Kokusho [35], analyses were conducted to determine the formation of dilating zone/water film beneath the lower permeability silty sand layer. The analysis confirmed the possible formation of the dilating zone/water film beneath the silty sand layer even during shaking which started decreasing after shaking stopped. This might have caused the shear deformation at the bottom of embedded silty sand layer in non-homogeneous and continuous layered foundation, inducing the deformation of embankment. Moreover, the dissipation of pore water from the underlying layer was concentrated at the discontinuous region below the embankment, inducing larger r_u values at P10 in NHG1 (Fig. 7). The larger r_u values can be attributed to the larger shear strain at different depths below the embankment centerline in Model NHG1 (Figs. 7 and 8(a)). A large shear strain below the embankment in Model NHG1 (Fig. 8(a)) indicated the larger lateral outflow of foundation soils and consolidation of loose sand below the embankment. This type of response has been investigated by many researchers and highlighted as the prime factor to embankment settlement and lateral deformation [31-33]. The crest settlement of Model NHG2 was not compared with the other tests as the intensity of applied input motion was smaller than that for the other tests.

The settlement occurred during the quite period between mainshock and aftershock (40-140 s) was nearly the same for all the models except Model NHG2 (Table 3). Our previous study [13] has shown that despite the fact that settlement during shaking was the same for different ground conditions, settlement induced by seepage after the shaking was found to be larger in non-homogeneous soil deposits. Figure 17 shows the displacement times histories at LV2 for Models NHG1 and NHG2. It is noted that the large difference in settlement during the mainshock (0-40 s) is due to the difference in the intensity of input motion. However, despite the application of low intensity input motion, the settlement induced by seepage after the mainshock (during 40-140 s) is larger in Model NHG2. Moreover, the settlement keeps increasing continuously with time during 40-140 s in Model NHG2 as shown in Fig. 17. Nonetheless, the settlement remains relatively constant for 110-140 s in Model NHG1. In addition, the Δu under the toe at P11 was larger during and after shaking in Model NHG2 than that in Model NHG1. The discontinuity in silty layer was below embankment toe (exactly below P11) in NHG2, causing larger Δu (Fig. 9). Had the intensity of input motion been the same for Models NHG1 and NHG2, the embankment settlement and lateral deformation at the toe in Model NHG2 might have been larger.

Similar to the mainshock, the crest settlement due to aftershock was also larger in Model NHG1 compared to other models (Table 3). In addition, the settlement induced due to seepage after shaking (160-1400 s) was significantly larger in Models NHG1 and CG compare to that in Model UG (Table 3). Figure 16(b) depicts the normalized crest settlements due to aftershock and complete dissipation of Δu for all the tests. The left vertical axis represents the normalized crest settlements relative to Model NHG1-MS and the right vertical axis represents the normalized crest settlements relative to Model UG. Dissipation of Δu became the major factor after the

shaking stopped, which caused some additional settlement. The crest settlement induced by dissipation of Δu after shaking is about 0.04 m in Model NHG1-MS. The crest settlement due to small aftershock and dissipation of Δu after shaking for Models UG, CG, and NHG1 was about 2.5, 2.8, and 3.5 times more than that for Model NHG1-MS, respectively. A small aftershock generated the additional Δu and accumulated shear strain ultimately increasing the displacements of the embankment (Figs. 8(b), 9, 14). Also, the crest settlement due to aftershock and pore water dissipation after shaking for Models NHG1 and CG was about 30% and 10% larger than that in Model UG, respectively. Model UG, consisting of a high permeability Toyoura sand foundation has faster dissipation of pore water while the dissipation continued for a longer time period in Models CG and NHG1, accumulating delayed displacements (Figs. 9 and 14).

5. Summary and Conclusions

A series of dynamic centrifuge tests was performed to investigate the seismic performance of earthen embankments resting on various liquefiable foundations. The liquefiable foundations include a uniform sand foundation, a multi-layered sand/silty sand foundation, and a non-homogeneous multi-layered discontinuous sand/silty sand foundation. The effects of repeated earthquake ground motions in the deformation of embankments were also studied by applying mainshock-aftershock sequential ground motions. The work presented in this study modeled the features of actual liquefiable soil profiles with discontinuous low permeability layers to provide new insights into the drainage path for dissipation of excess pore water pressure in various ground conditions and compared the liquefaction-induced deformation of embankments on different foundations.

Several conclusions can be drawn from the results of the model tests discussed in this paper. Clear shear straining was observed in the foundation and the embankments appeared to have settled into the foundation in all tests. The accumulation of pore water beneath the low permeability silty sand layer induced large shear strain below the silty sand layer, resulting lateral spreading and excessive settlement in non-homogeneous foundation. In the non-homogeneous foundation, the dissipation of pore water from the underlying layer was concentrated at the discontinuous region below the embankment, inducing the larger excess pore water pressure ratios. No massive failures were observed in the embankments, but the overall deformation was still very large in the non-homogeneous foundation. Severe deformation patterns in the form of cracking, lateral spreading and slumping were observed. It was found that the sequential ground motions have a significant effect on the accumulated deformation of embankments. Moreover, the effects of aftershocks were more pronounced in the non-homogeneous liquefiable foundations, leading to the post-liquefaction delayed settlement. This study modeled the multi-layered soil profile consisting of discontinuous thin layers of low permeability based on observations of several damage sites during recent earthquakes to improve the ability to account for them in practice. The test results would be useful in the development of design guidelines, as well as in the calibration of numerical procedures.

Acknowledgements

Support for the first author is provided by a Monbukagakusho (Ministry of Education, Culture, Sports, Science and Technology, Japan) scholarship for graduate students. The work presented in this paper is a part of the research and development project on safety measures for levees, commissioned by the Ministry of Land, Infrastructure, Transport and Tourism, Japan.

References

[1] Seed HB. Landslides during earthquakes due to liquefaction, Journal of Soil Mechanics & Foundations Div 1968;94(5):1055-123.
[2] Koga Y, Matsuo O. Shaking table tests of embankments resting on liquefiable sandy ground, Soils and Foundations 1990;30(4):162-74.
[3] Matsuo O. Damage to river dikes, Soils and Foundations 1996:235-40.
[4] Adalier K, Elgamal AW, Martin GR. Foundation liquefaction countermeasures for earth embankments, Journal of Geotechnical and Geoenvironmental Engineering 1998;124(6):500-17.
[5] Tani S. Consideration of earthquake damage to earth dam for irrigation in Japan, Proc. 2nd Intl. Conf. on Recent Advances in Geotechnical Earthquake Engineering and Soil Dynamics, 1991;1137-42.
[6] Aydingun O, Adalier K. Numerical analysis of seismically induced liquefaction in earth embankment foundations. Part I. Benchmark model, Canadian Geotechnical Journal 2003;40(4):753-65.
[7] Adalier K, Sharp MK. Embankment dam on liquefiable foundation-dynamic behavior and densification remediation, Journal of Geotechnical and Geoenvironmental Engineering 2004;130(11):1214-24.
[8] Kokusho T. Water film in liquefied sand and its effect on lateral spread, Journal of Geotechnical and Geoenvironmental Engineering 1999;125(10):817-26.
[9] Kokusho T. Mechanism of water film generation and lateral flow in liquified sand layer, Soils and Foundations 2000;40(5):99-111.
[10] Malvick EJ, Kutter BL, Boulanger RW. Postshaking shear strain localization in a centrifuge model of a saturated sand slope, Journal of Geotechnical and Geoenvironmental Engineering 2008;134:164-74.
[11] Kulasingam R, Malvick EJ, Boulanger RW, Kutter BL. Strength loss and localization at silt interlayers in slopes of liquefied sand, Journal of Geotechnical and Geoenvironmental Engineering 2004;130(11):1192-202.
[12] Maharjan M, Takahashi A. Effects of non-homogeneity on liquefaction in stratified soil deposits, Proceeding of Tenth International Conference for Urban Earthquake Engineering, Tokyo, Japan, 2013;483-92.
[13] Maharjan M, Takahashi A. Centrifuge model tests on liquefaction-induced settlement and pore water migration in non-homogeneous soil deposits, Soil Dynamics and Earthquake Engineering 2013;55:161-69.
[14] Oka F, Tsai P, Kimoto S, Kato R. Damage patterns of river embankments due to the 2011 off the Pacific Coast of Tohoku earthquake and a numerical modeling of the deformation of river embankments with a clayey subsoil layer, Soils and Foundations 2012;52(5):890-909.
[15] GEER. Quick Report 2: Preliminary Observations of Levee Performance and Damage following the March 11, 2011 Tohoku Offshore Earthquake, Japan, Geotechnical Extreme Events Reconnaissance (GEER) Association 2011.
[16] Zhang S, Wang G, Sa W. Damage evaluation of concrete gravity dams under mainshock–aftershock seismic sequences, Soil Dynamics and Earthquake Engineering 2013;50:16-27.
[17] Okamura M, Abdoun TH, Dobry R, Sharp MK, Taboda VM. Effects of sand permeability and weak aftershocks on earthquake-induced lateral spreading, Soils and Foundations 2001;41(6):63-77.
[18] Meneses-Loja J, Ishihara K, Towhata I. Effects of superimposing cyclic shear stress on the undrained behavior of saturated sand under monotonic loading, Soils and Foundations 1998;38(4):115-27.
[19] Ishihara K, Cubrinovski M. Problems associated with liquefaction and lateral spreading during earthquakes, Geotechnical Earthquake Engineering and Soil Dynamics III 1998;75(1):301-12.
[20] Ye B, Ye G, Zhang F, Yashima A. Experiment and numerical simulation of repeated liquefaction-consolidation of sand, Soils and Foundations 2007;47(3):547-58.

[21] Xia Z-F, Ye G-L, Wang J-H, Ye B, Zhang F. Fully coupled numerical analysis of repeated shake-consolidation process of earth embankment on liquefiable foundation, Soil Dynamics and Earthquake Engineering 2010;30(11):1309-18.
[22] Sasaki Y, Towhata I, Miyamoto K, Shirato M, Narita A, Sasaki T, Sako S. Reconnaissance report on damage in and around river levees caused by the 2011 off the Pacific coast of Tohoku earthquake, Soils and Foundations 2012;52(5):1016-32.
[23] Atkinson J. The mechanics of soils and foundations, Taylor and Francis, London and New York, 2007.
[24] Kishida H. Damage to reinforced concrete buildings in Niigata City with special reference to foundation engineering, Soils and Foundations 1966;6(1):71-88.
[25] PEER. Pacific Earthquake Engineering Research (PEER) Center: Ground Motion Database; 2013. <http://peer.berkeley.edu/peer_ground_motion_database>.
[26] Osterberg JO. Influence values for vertical stresses in semi-infinite mass due to embankment loading, Proceedings of the 4th Internationa Conference on Soil Mechanics and Foundation Engineering, London, 1957;1:393-96.
[27] Boulanger RW, Seed RB. Liquefaction of sand under bidirectional monotonic and cyclic loading, Journal of Geotechnical Engineering 1995;121(12):870-78.
[28] Ishihara K, Yamazaki F. Cyclic simple shear tests on saturated sand in multi-directional loading, Soils and Foundations 1980;20(1):45-59.
[29] Dobry R, Liu L. Centrifuge modeling of soil liquefaction, Tenth World Conference on Earthquake Engineering, 1992;6801-09.
[30] Liu L, Dobry R. Seismic response of shallow foundation on liquefiable sand, Journal of Geotechnical and Geoenvironmental Engineering 1997;123(6):557-67.
[31] Dobry R, Taboada V, Liu L. Centrifuge modeling of liquefaction effects during earthquakes, Proceedings 1st International Conference on Earthquake Geotechnical Engineering, Rotterdam, The Netherlands, 1995;129-62.
[32] Elgamal AW, Zeghal M, Taboda V, Dobry R. Analysis of site liquefaction and lateral spreading using centrifuge testing records, Soils and Foundations 1996;36(2):111-21.
[33] Okamura M, Matsuo O. Effects of remedial measures for mitigating embankment settlement due to foundation liquefaction, International Journal of Physical Modelling in Geotechnics 2002;2(2):1-12.
[34] Sharp MK, Adalier K. Seismic response of earth dam with varying depth of liquefiable foundation layer, Soil Dynamics and Earthquake Engineering 2006;26(11):1028-37.
[35] Kokusho T. Mechanism for water film generation and lateral flow in liquefied sand layer, Soils and Foundations 2000;40(5):99-111.

Table 1 Index properties of soils

Property	Toyoura sand	Silica sand No. 8
Specific gravity, G_s	2.65	2.65
D_{50} (mm)	0.19	0.10
D_{10} (mm)	0.14	0.041
Maximum void ratio, e_{max}	0.973	1.333
Minimum void ratio, e_{min}	0.609	0.703
Permeability, k (m/s) at Dr=50%	2×10^{-4}	2×10^{-5}
Sand %	100%	75%
Silt%		25%

Table 2 Summary of model configurations

Test code	Model series	Peak acceleration of input motion (g)	
		Mainshock	Aftershock
Model NHG1	Non-homogeneous foundation with discontinuity below the center of embankment at shallow depth	0.43	0.24
Model NHG2	Non-homogeneous foundation with discontinuity below the toe of embankment at shallow depth	0.37	0.16
Model UG	Uniform sand foundation	0.43	0.27
Model CG	Continuous silty sand layered foundation	0.43	0.28

Table 3 Crest settlement during various time stages

Model	Crest settlement (mm)			
	0-40 s[a]	40-140 s[b]	140-160 s[c]	160-1400 s[d]
NHG1	341.7	30.7	49.3	65.0
NHG2	258.5	34.8	13.7	33.1
UG	280.0	29.1	41.3	30.2
CG	314.7	29.6	43.6	62.1
NHG1-MS	335.3		40.9[*]	

Time period: [a]Mainshock event; [b]Quite period between mainshock and aftershock; [c]Aftershock event; [d]After shaking until complete dissipation of pore water

[*]Crest settlement after mainshock, i.e., 40-1400 s

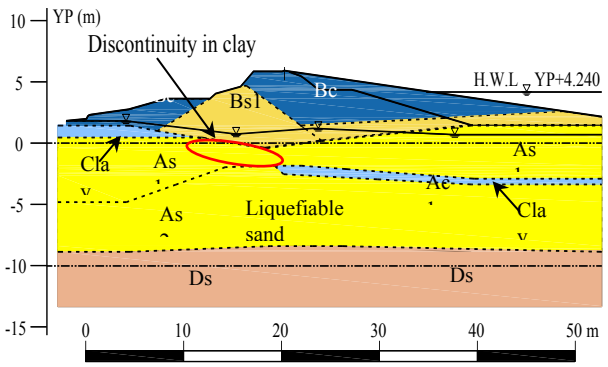

Fig. 1. Non-homogeneous soil profile along levee in Tone River (Left levee at 32.3 km) (courtesy of Kanto Regional Development Bureau of Ministry of Land, Infrastructure, Transport and Tourism, Japan)

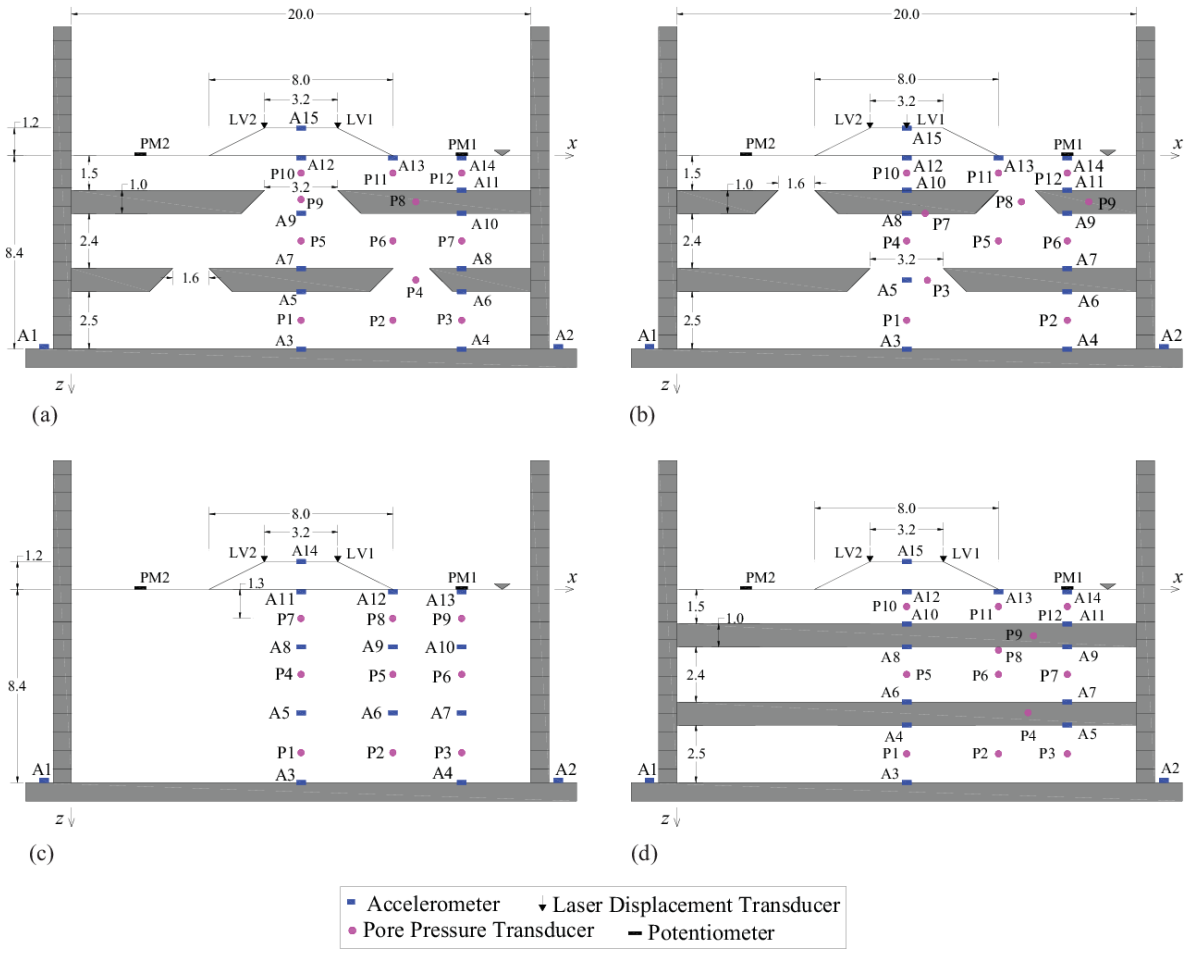

Fig. 2. Model test configurations: (a) Model NHG1, (b) Model NHG2, (c) Model UG, and (d) Model UG (All the units are in meters in the prototype scale)

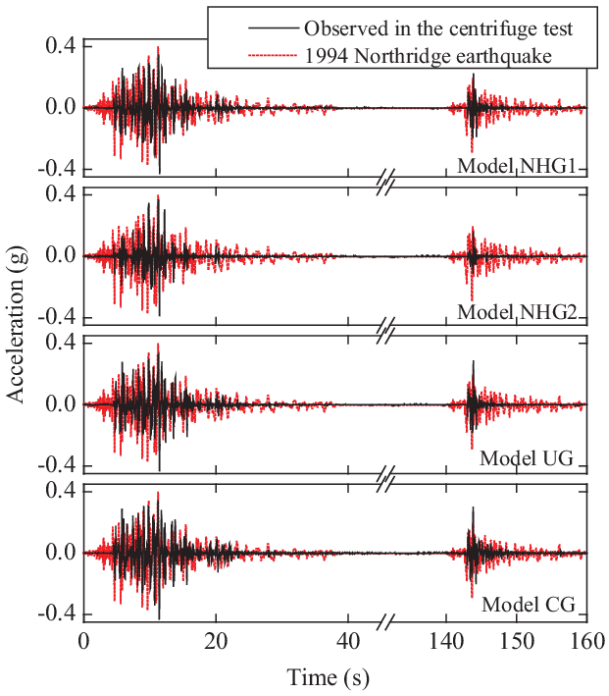

Fig. 3. Acceleration time histories of input base motion

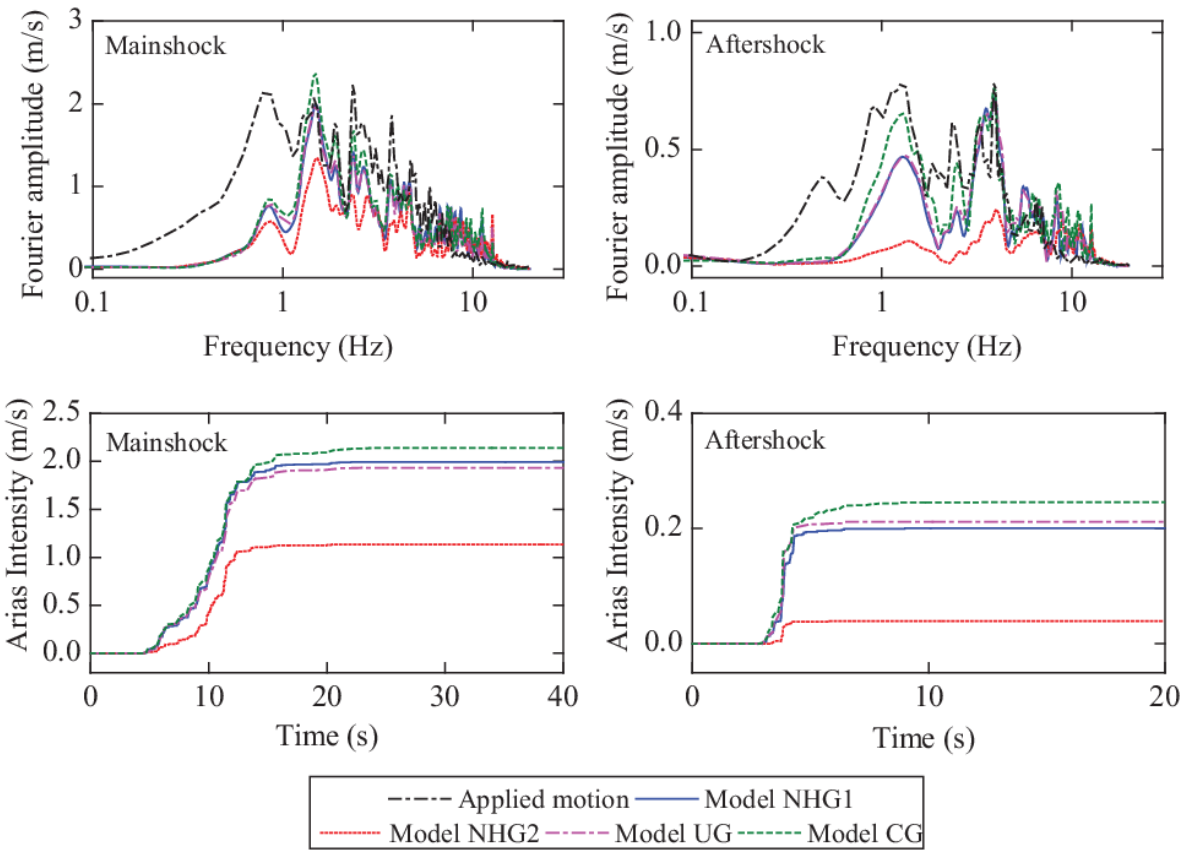

Fig. 4. Fourier spectra and Arias intensities of input base motion

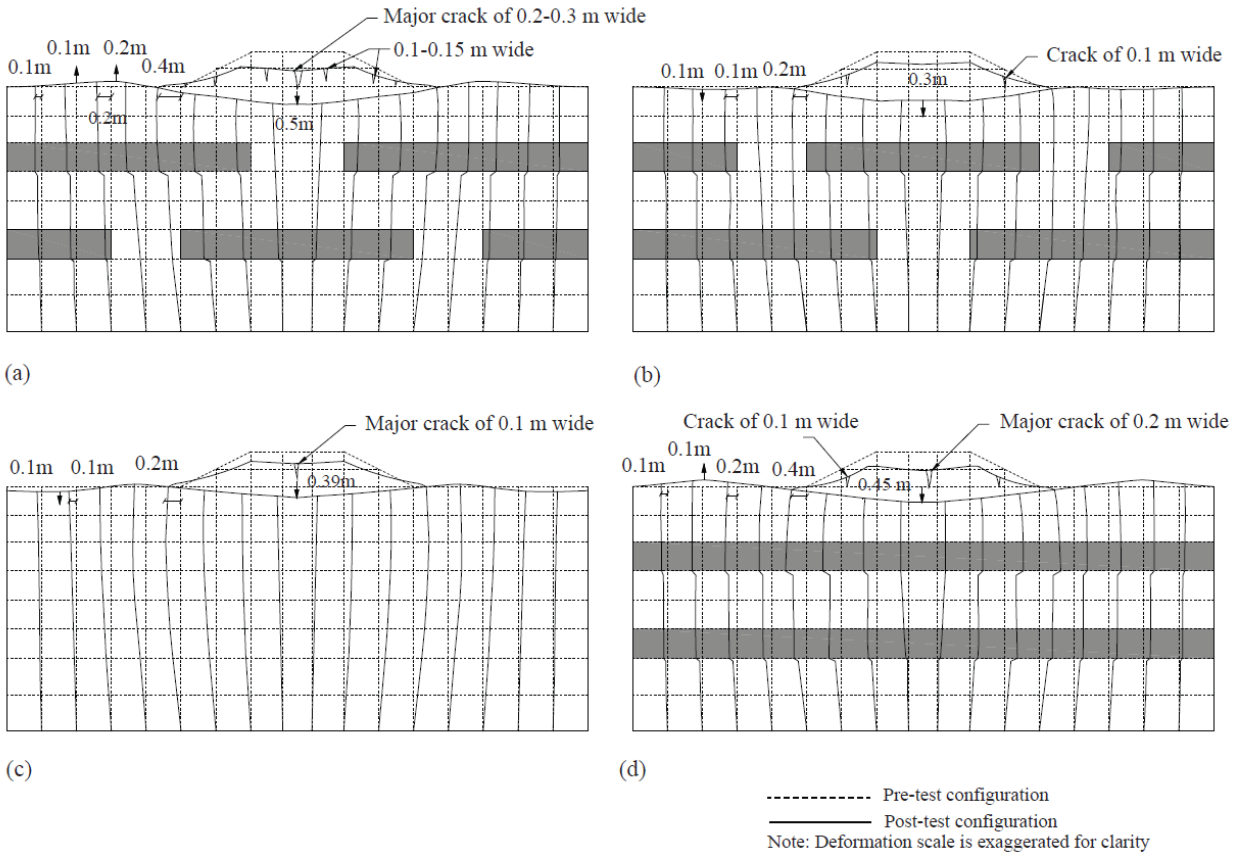

1

2 Fig. 5. Deformed shape of (a) Model NHG1, (b) Model NHG2, (c) Model UG, and (d) Model UG

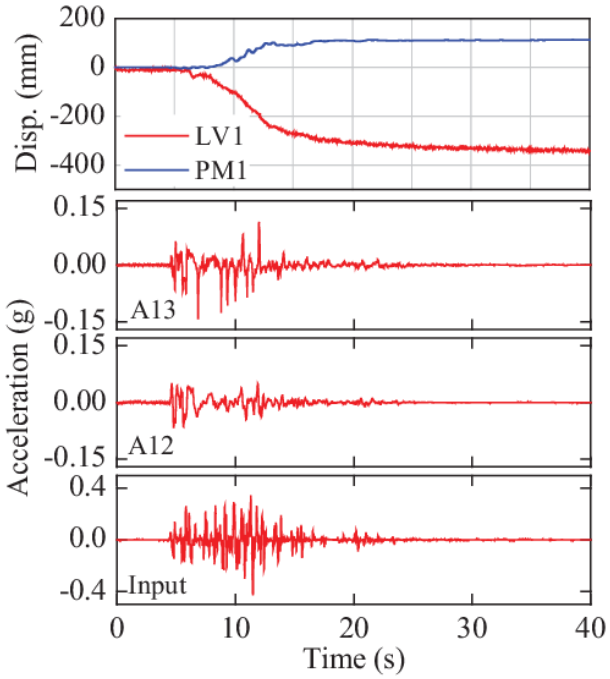

3

4 Fig. 6. Time histories of displacements and accelerations in Model NHG1

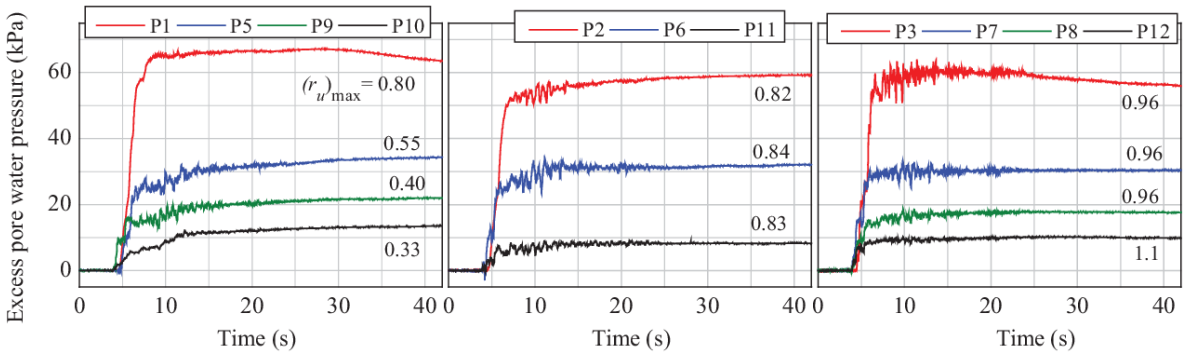

Fig. 7. Time histories of excess pore water pressure at selected locations during mainshock in Model NHG1 (The numbers on figures represent the maximum r_u values)

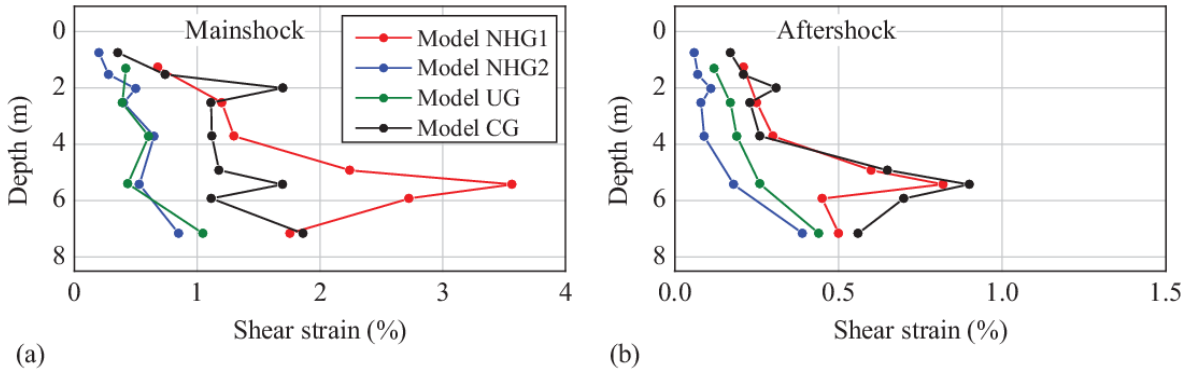

Fig. 8. Maximum shear strain amplitude in centerline at different depths: (a) Mainshock and (b) Aftershock

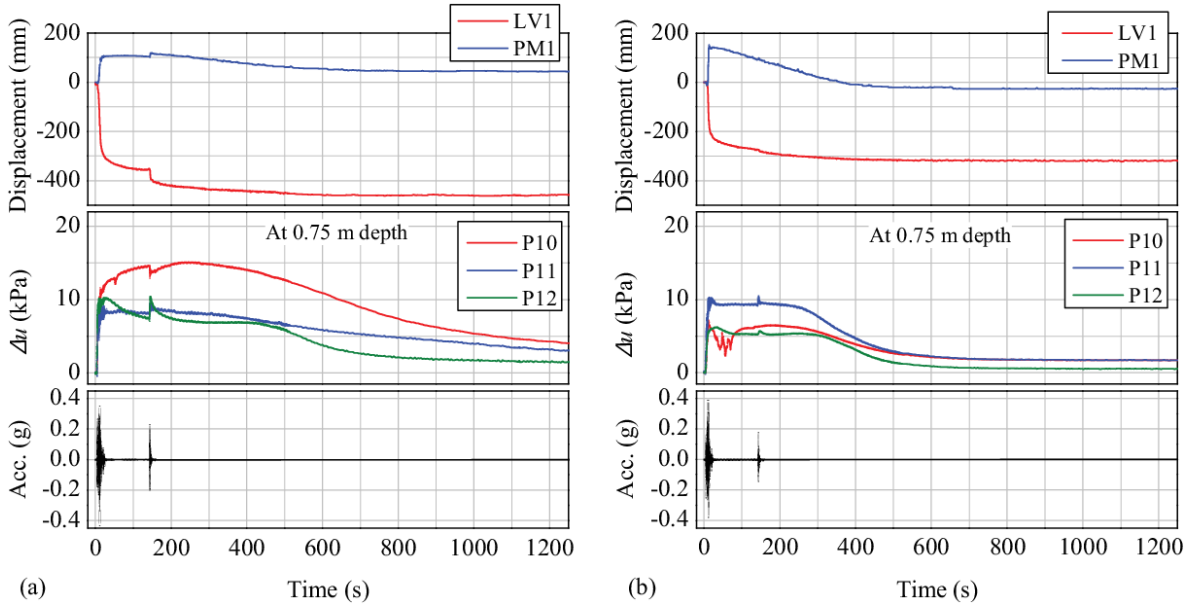

Fig. 9. Time histories of input acceleration, excess pore water pressure (Δu), and displacement during and after shaking: (a) Model NHG1 and (b) Model NHG2

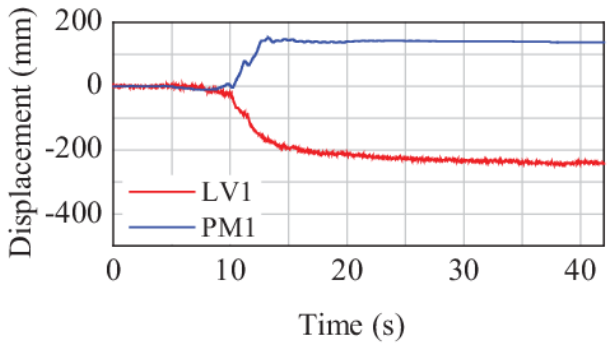

Fig. 10. Displacement time histories at LV1 and PM1 in Model NHG2

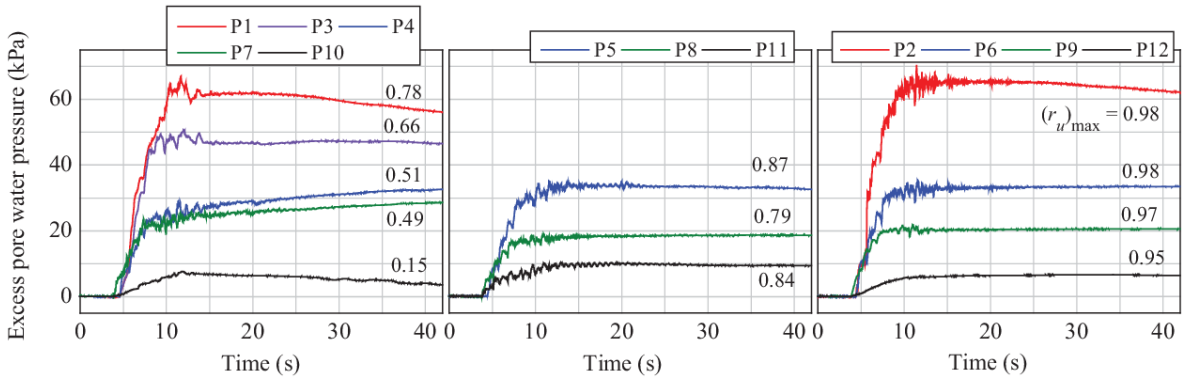

Fig. 11. Time histories of excess pore water pressure at selected locations during mainshock in Model NHG2 (The numbers on figure represent the maximum r_u values)

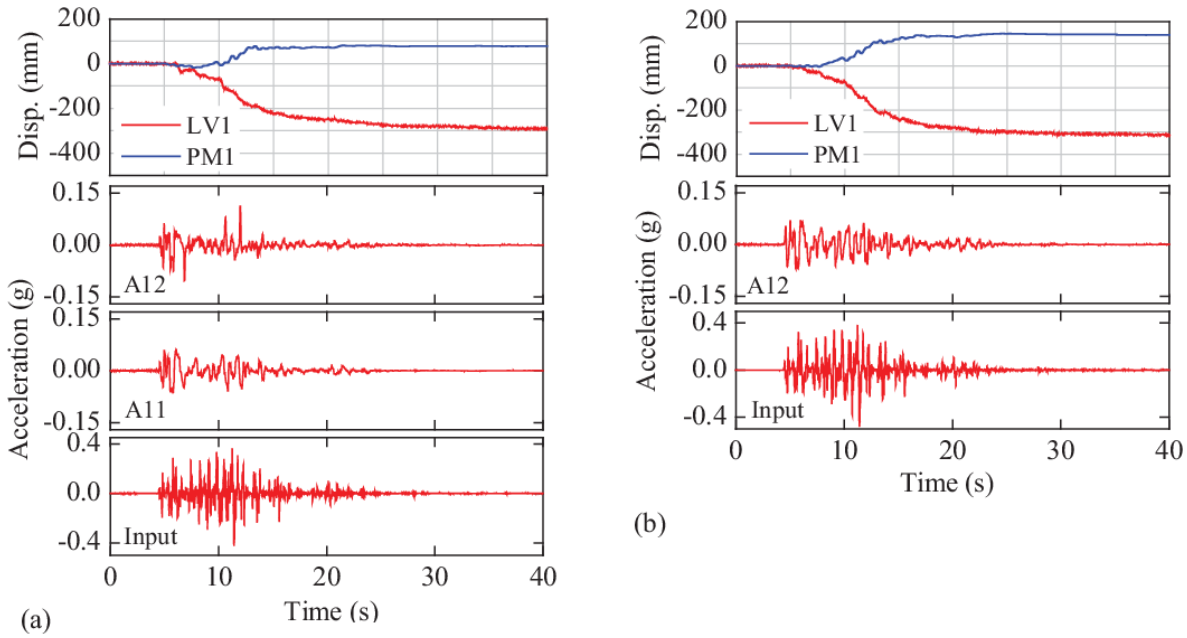

Fig. 12. Time histories of displacement and accelerations: (a) Model UG and (b) Model CG

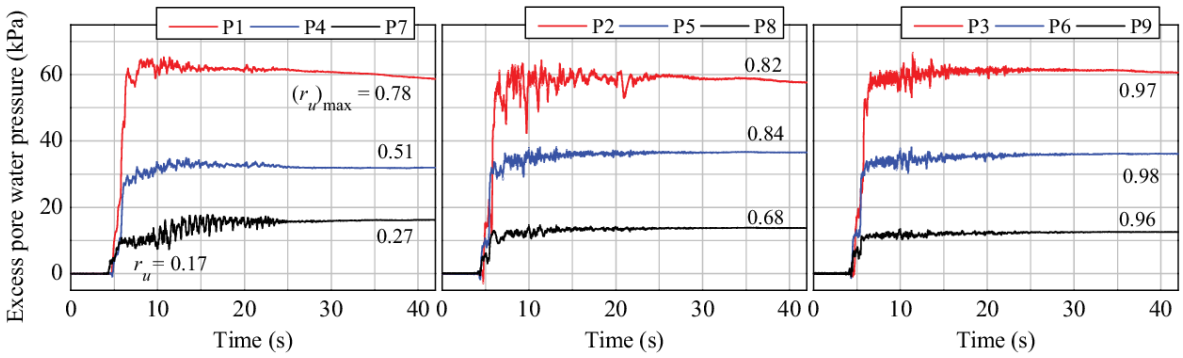

Fig. 13. Time histories of excess pore water pressure at selected locations during mainshock in Model UG (The numbers on figure represent the maximum r_u values)

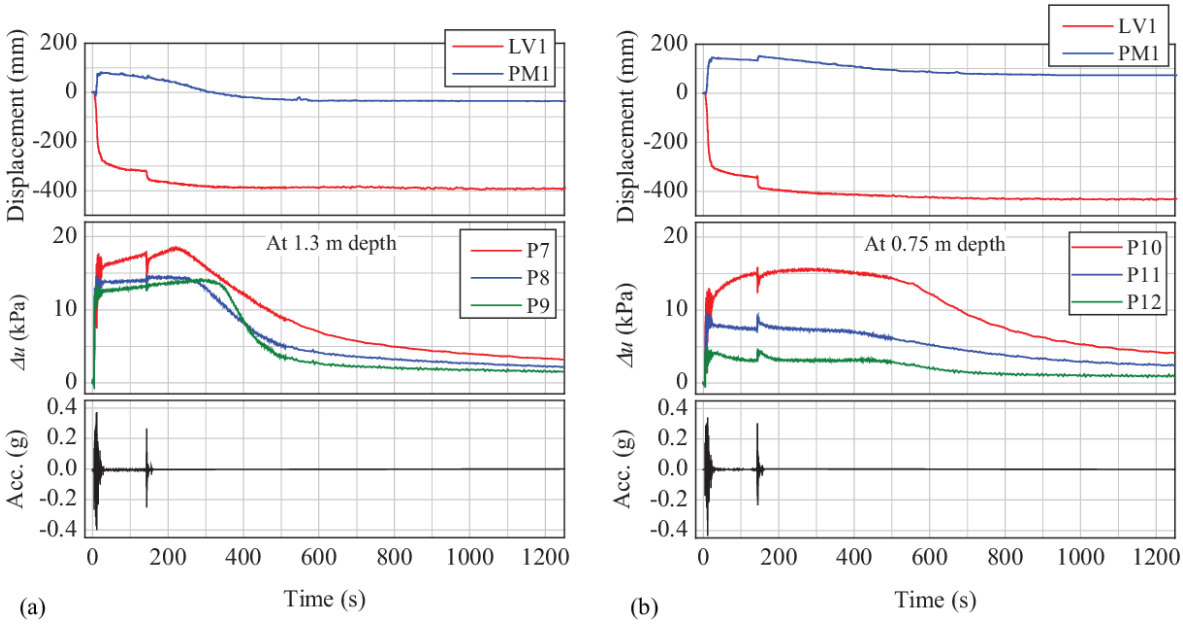

Fig. 14. Time histories of input acceleration, excess pore water pressure (Δu), and displacement during and after shaking: (a) Model UG and (b) Model CG

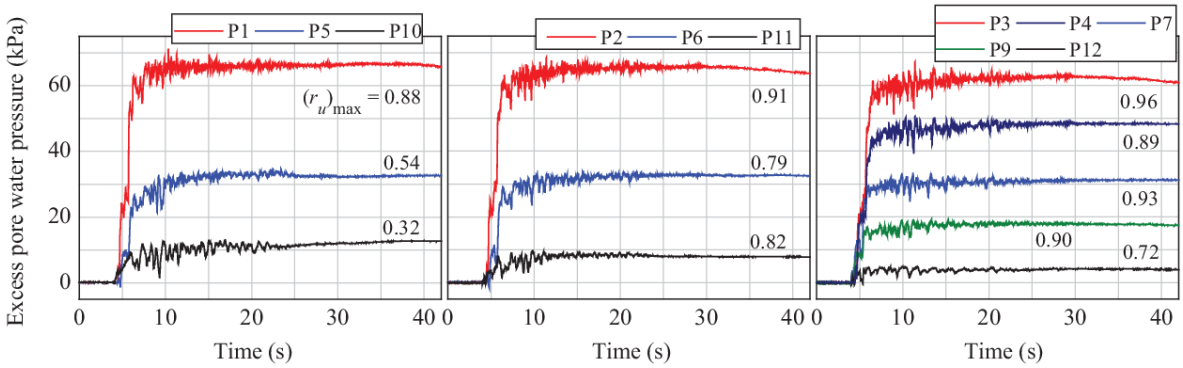

Fig. 15. Time histories of excess pore water pressure at selected locations during mainshock in Model CG (The numbers on figure represent the maximum r_u values)

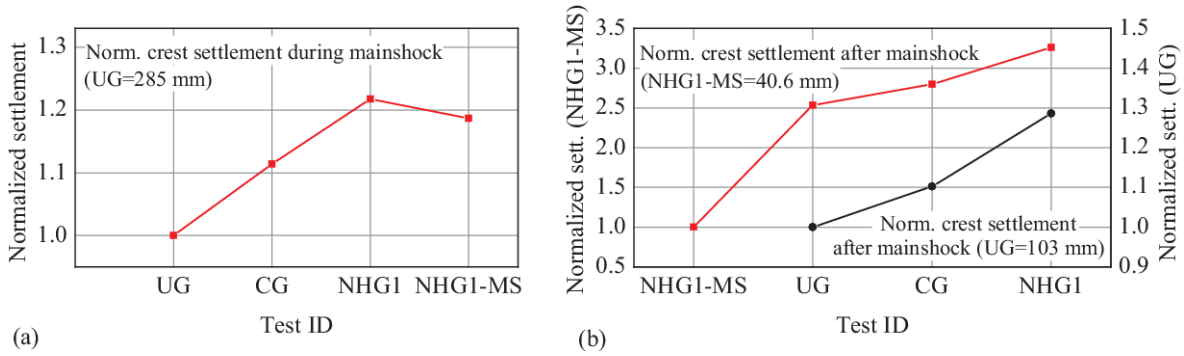

Fig. 16. Normalized crest settlement: (a) During mainshock and (b) During aftershock and total dissipation of excess pore water pressure

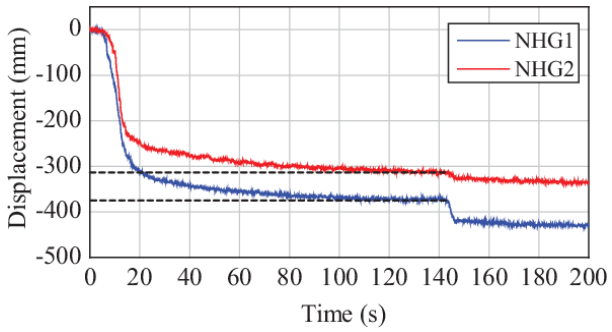

Fig. 17. Displacement time histories at LV2 for Models NHG1 and NHG2